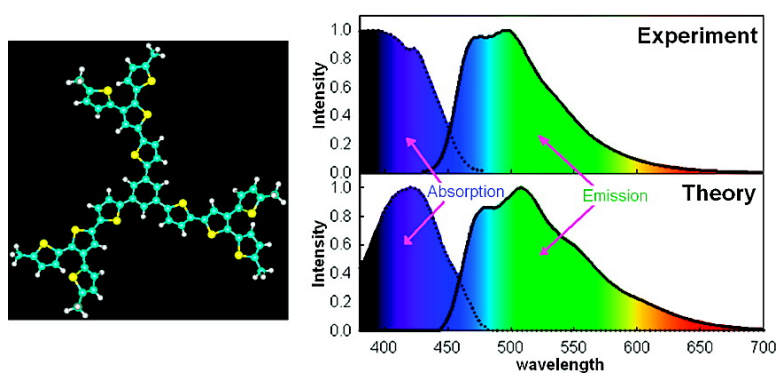Article

Theoretical Studies on Conjugated Phenyl-Cored Thiophene Dendrimers for Photovoltaic Applications

Muhammet E. Kse, William J. Mitchell, Nikos Kopidakis, Christopher
H. Chang, Sean E. Shaheen, Kwiseon Kim, and Garry Rumbles

More About This Article

Additional resources and features associated with this article are available within the HTML version:

- Supporting Information
- Links to the 8 articles that cite this article, as of the time of this article download
- Access to high resolution figures
- Links to articles and content related to this article
- Copyright permission to reproduce figures and/or text from this article

View the Full Text HTML

Theoretical Studies on Conjugated Phenyl-Cored Thiophene Dendrimers for Photovoltaic Applications

Muhammet E. Köse,* William J. Mitchell, Nikos Kopidakis, Christopher H. Chang, Sean E. Shaheen, Kwiseon Kim, and Garry Rumbles

Contribution from the National Renewable Energy Laboratory, 1617 Cole Boulevard, Golden, Colorado 80401-3393

Received May 15, 2007; E-mail: muhammet_kose@nrel.gov

Abstract: π-Conjugated dendrimers are an important class of materials for optoelectronic devices, especially for light-harvesting systems. We report here a theoretical investigation of the optical response and of the excited-state properties of three-arm and four-arm phenyl-cored dendrimers for photovoltaic applications. A variety of theoretical methods are used and evaluated against each other to calculate vertical transition energies, absorption and excitation spectra with vibronic structure, charge transport, and excitonic behavior upon photoexcitation and photoemission processes. Photophysical phenomena in these dendrimers are, in general, better explained with *ab initio* methods rather than with semiempirical techniques. Calculated reorganization energies were found to correlate well with the device photocurrent data where available. The excitons formed during photoexcitation are calculated to be more delocalized than the ones formed after vibrational relaxation in the excited states for fluorescence emission. The localization of excitons in emission processes is a result of geometrical changes in the excited state coupled with vibronic modes. Correlated electron–hole pair diagrams illustrate breaking of π-conjugation in three-arm dendrimers due to meta linkage of arms with the core, whereas four-arm dendrimers are not affected by such breaking due to presence of ortho and para branching. Yet, ortho branching causes large twist angles between the core and the arms that are detrimental to π-electron system delocalization over the structure.

1. Introduction

The key parameter that controls the photophysical and the optical properties of conjugated polymers and oligomers is their extended, polarizable, and mobile π-electron system along the conjugated backbone. In recent years, there is considerable research effort to utilize conjugated polymers and related systems in organic photovoltaic (OPV) applications.[1,2] Polymer synthesis, in general, results in chains of various sizes, and the chains with different molecular weight can significantly alter the carrier mobility when used in OPV devices.[3,4] Therefore, monodispersed materials are desired in bulk heterojunction OPV applications due to the ability to control the morphology of blends, which has been shown to be an important factor for efficient charge transport and device efficiency.[5] In this regard, conjugated dendrimers offer an alternative to the conjugated polymers that are extensively used in organic solar cells.[6] Dendrimers (1) possess the advantage of having a well-defined

molecular weight compared to polymers; (2) have improved batch-to-batch reproducibility; and (3) can be synthesized with high purity compared to polymers. In addition, conjugated dendrimers are expected to show a high degree of ordering in OPV devices due to their small size and monodisperse nature. It has already been shown in organic light-emitting diodes that dendrimers can efficiently transport charge and also form high quality films.[7] In particular, Xia et al. synthesized thiophene dendrons and dendrimers in various sizes[8] and demonstrated the ability of thiophene dendrimers to form ordered structures such as nanowires and 2D crystals on specific surfaces.[9]

To utilize π-conjugated dendrimers in OPV applications, we have previously synthesized and characterized phenyl-cored thiophene dendrimers with three (1, 3, 5 positions) and four (1, 2, 4, 5 positions) arms attached around the core (Figure 1).[10] A convergent synthesis method was employed to assemble the dendrimers from the outside through to termination at the core. The nomenclature used for the dendrimers is given in Figure 1: mGp-nS, where m is the number of arms, p is the generation number, and n is the number of thiophenes between the core and the surface group, within each arm. Optical band gaps of dendrimers (varied between 2.10 and 2.55 eV) were decreased

(1) Shaheen, S. E.; Ginley, D. S.; Jabbour, G. E. *MRS Bull.* **2005**, *30*, 10−19.
(2) Gledhill, S. E.; Scott, B.; Gregg, B. A. *J. Mater. Res.* **2005**, *20*, 3167−3179.
(3) Kline, R. J.; McGehee, M. D.; Kadnikova, E. N.; Liu, J. S.; Fréchet, J. M. J. *Adv. Mater.* **2003**, *15*, 1519−1522.
(4) Schilinsky, P.; Asawapirom, U.; Scherf, U.; Biele, M.; Brabec, C. J. *Chem. Mater.* **2005**, *17*, 2175−2180.
(5) Yang, X. N.; Loos, J.; Veenstra, S. C.; Verhees, W. J. H.; Wienk, M. M.; Kroon, J. M.; Michels, M. A. J.; Janssen, R. A. J. *Nano Lett.* **2005**, *5*, 579−583.
(6) Kopidakis, N.; Mitchell, W. J.; van de Lagemaat, J.; Ginley, D. S.; Rumbles, G.; Shaheen, S. E.; Rance, W. L. *Appl. Phys. Lett.* **2006**, *89*, 103524−103526.

(7) Lo, S. C.; Burn, P. L. *Chem. Rev.* **2007**, *107*, 1097−1116.
(8) Xia, C. J.; Fan, X. W.; Locklin, J.; Advincula, R. C. *Org. Lett.* **2002**, *4*, 2067−2070.
(9) Xia, C. J.; Fan, X. W.; Locklin, J.; Advincula, R. C.; Gies, A.; Nonidez, W. *J. Am. Chem. Soc.* **2004**, *126*, 8735−8743.
(10) Mitchell, W. J.; Kopidakis, N.; Rumbles, G.; Ginley, D. S.; Shaheen, S. E. *J. Mater. Chem.* **2005**, *15*, 4518−4528.
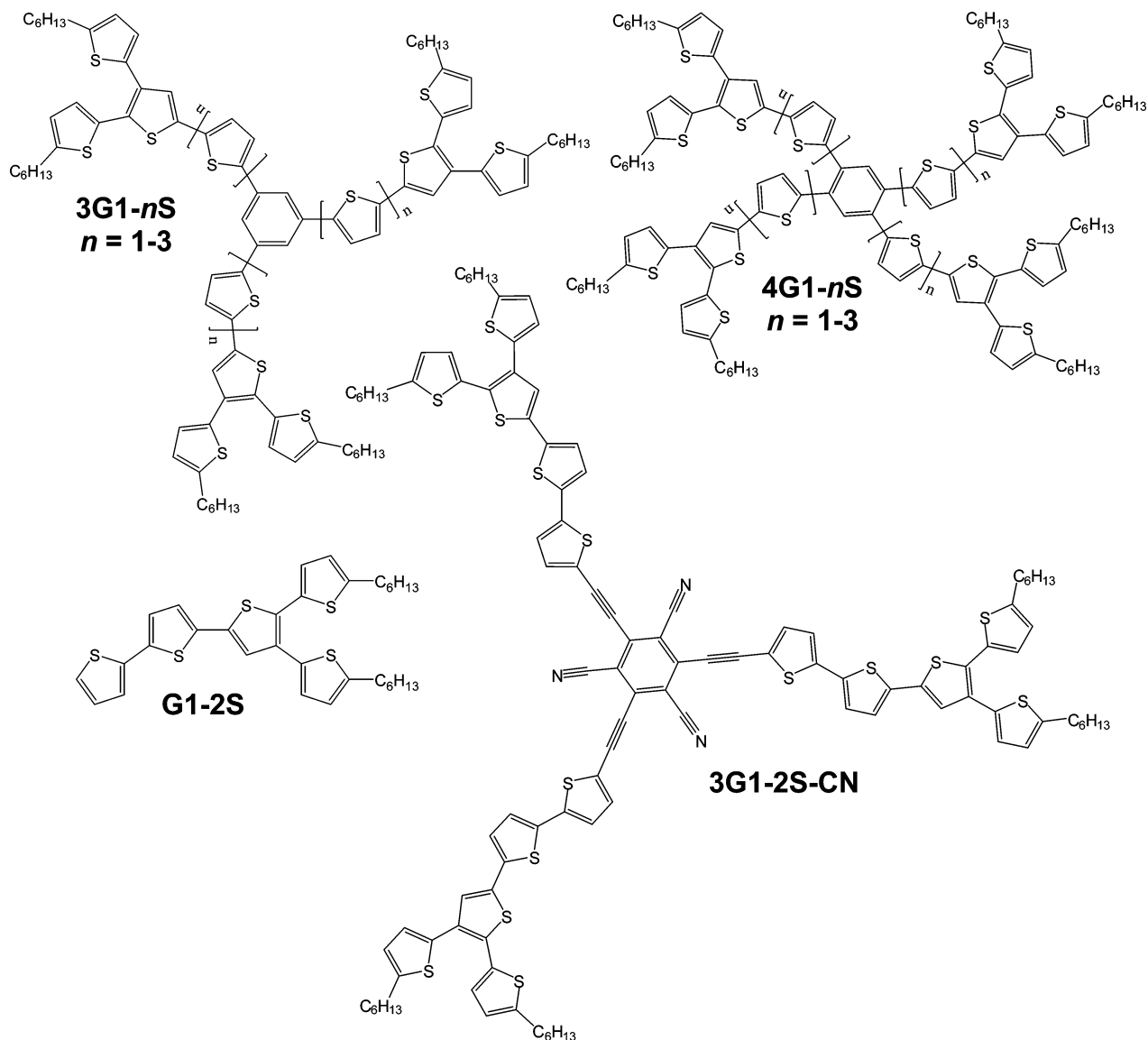
Figure 1. Chemical structure of phenyl-cored dendrimers and G1-2S molecule.

with the increasing number of thiophenes (*n*) in the arms due to extended π-system conjugation over the molecular structure.[10] To further decrease the band gap, 3G1-2S-CN was synthesized by addition of electron-withdrawing cyano groups to the 2, 4, and 6 positions on the phenyl core that were not occupied by arms. Acetylene groups were inserted between the core and the thiophene segment to decrease the effect of steric repulsion between the arms (Figure 1). Our attempts to exploit phenyl-cored thiophene dendrimers as donor materials (with acceptor [6,6]-phenyl C_{60} butyric acid methyl ester (PCBM)) in bulk heterojunction photovoltaic devices gave promising 1.3% power conversion efficiency with a 4G1-3S dendrimer for an unoptimized band gap for light harvesting.[6]

To gain more understanding of the electronic properties of these materials, we used several *ab initio* (HF, RCIS, DFT,[11] TD−DFT)[12] and semiempirical (AM1, AM1-CI, PM3, PM3-CI, ZINDO)[13] methods to predict the optical properties, charge

transport, and degree of excitonic localization (or delocalization) in these relatively large molecules. The theoretical findings on the optical properties agree well with the experiment. The predictive power of semiempirical methods was compared and evaluated against the *ab initio* ones, with the latter performing better. A rigorous Franck−Condon calculation also allowed us to simulate the vibronic progression in the optical spectra. Reorganization energies in charge transport calculations were found to correlate well with experimental short-circuit current data in devices.[6] ZINDO calculations were performed to shed light on spatial location of excitons that are formed in photoexcitation and photoemission processes.

2. Experimental Section

The synthesis and characterization of the structures in Figure 1 are given in detail elsewhere.[10] All absorption spectra of dendrimers and

(11) There is still debate over whether DFT is an *ab initio* method considering the parameters used in the development of functionals. However, DFT uses far fewer parameters than other semiempirical methods, and therefore, we classify it as an *ab initio* technique.

(12) HF, Hartree−Fock; RCIS, restricted configuration interaction singles; DFT, density functional theory; TD-DFT, time-dependent density functional theory.

(13) AM1, Austin model 1; AM1-CI, AM1 model coupled with full configuration interaction scheme; PM3, parametrized method 3; PM3-CI, PM3 model coupled with full configuration interaction scheme; ZINDO, Zerner's intermediate neglect of differential overlap.
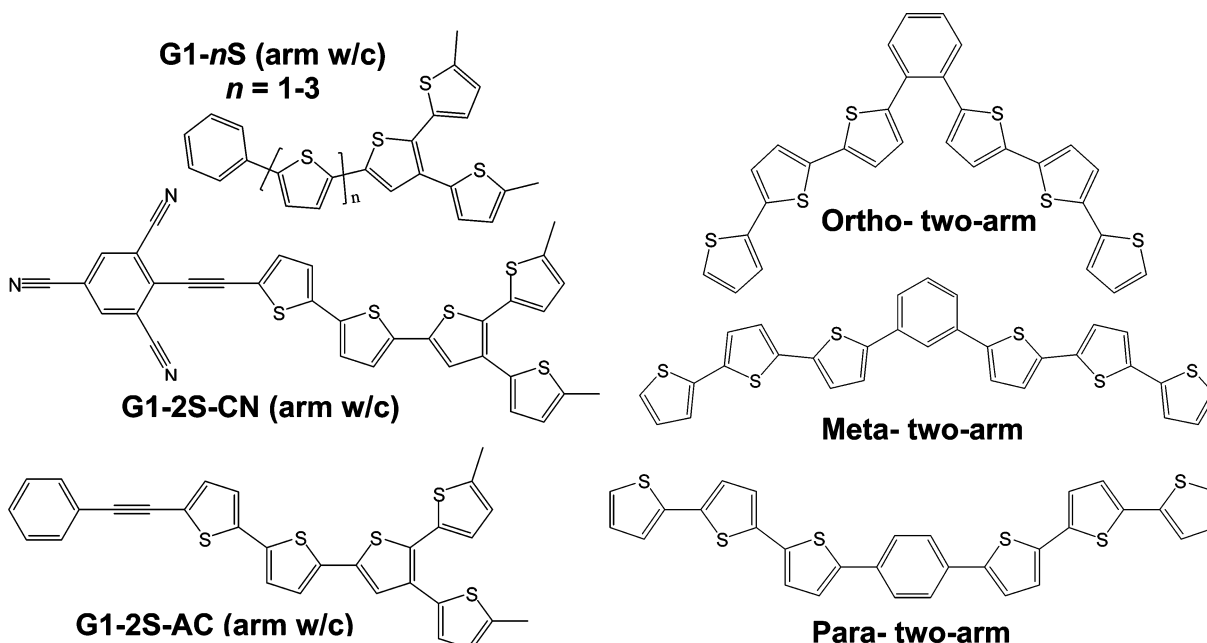
Figure 2. Dendrimer arms with core and two-arm phenyl-cored structures with ortho, meta, and para substitutions used in theoretical calculations.

of G1-2S were taken as solutions in dicholoromethane (DCM), in tetrahydrofuran (THF), or in 2-methyl THF (for low temperature measurements) using a Cary 500 spectrophotometer. Steady-state photoluminescence spectra were recorded on a spectrometer (JY Horiba Fluorolog 3) with a 450 W xenon arc lamp and double monochromator as the excitation source. Emission was observed at right angles to excitation through a spectrograph and detected using a cooled (140 K) CCD multichannel detector. A nitrogen-cooled cryostat (Oxford Instruments) was used to collect the spectra of 2-methyl THF solutions of dendrimers at 80 Kelvin. The solvent, 2-methyl THF, freezes below 137 K. All spectra were corrected for the intensity of the excitation lamp and the wavelength-dependence of the detection system.

3. Theoretical Approaches

Computational Methods. To study absorption and emission behavior of structures in Figure 1, we employed both hybrid density functional theory (DFT) and spin-restricted configuration interaction with single excitations (RCIS) methods as implemented in the Gaussian 03 package.[14] Ground-state geometries were obtained at the B3LYP level of theory, which combines the Becke[15] exchange and Lee−Yang− Parr correlation functional[16] with an optimized weight of the exact HF exchange.[17] The 6-31G(d) split-valence polarized basis set was employed for these geometry optimizations. Excited-state structures of dendrimers were calculated with a RCIS/3-21G model chemistry within a limited active space. The size of the CI active space varied from 40 to 120 occupied and unoccupied molecular orbitals depending on the size of the calculated structure. To compare and understand the photophysics of dendrimers, we also performed calculations for the absorption/emission profiles of dendrimer arms of various sizes with the core attached to the arm (Figure 2). Vertical transition energies were obtained by using time-dependent density functional theory (TD− DFT) method, using B3LYP hybrid functional along with 6-31G(d) basis set. Ground-state structures of 3G1-nS were optimized by using C_3 symmetry, whereas C_2 symmetry was employed for 4G1-nS series of dendrimers. Excited-state geometry optimizations were carried out without any symmetry restrictions. In addition to DFT and RCIS

methods, we have determined the ground-state geometries of dendrimers with AM1 and PM3 semiempirical methods, as implemented in the AMPAC package.[18] Excited-state geometries were obtained in the lowest excited-state by coupling the AM1 model (AM1-CI) or PM3 model (PM3-CI) to a full CI scheme in a limited active space.

Radical cations and anions of representative structures were also computed using spin-unrestricted UB3LYP/6-31G(d) method wave functions without any symmetry restrictions imposed on the initial geometries. The largest value obtained for $\langle S^2 \rangle$ was 0.77 (0.75 is required for a doublet), indicating that spin contamination is nearly absent in these open-shell calculations. The results were used to generate excess charge distribution plots and to calculate the intramolecular reorganization energies of dendrimers in the charged state.

Vibronic Coupling. We have employed three different approaches for simulation of vibronic bands in selected structures. The ground-state [excited-state] structures and vibrational frequencies were obtained by HF/3-21G [RCIS/3-21G], AM1 [AM1-CI], and PM3 [PM3-CI] methods. All of the vibrational frequencies obtained from various methods were scaled by 0.9.[19] The vibronic spectra of G1-2S, 3G1-1S, and 4G1-1S were obtained by following the approach described by Gierschner et al.[20] This approach assumes a displaced, but undistorted, harmonic oscillator model to estimate vibrational progressions.[21] Briefly, the projection of geometry change between two states (i,f) can be calculated by

$$\Delta Q_k = [x_f - x_i]M^{1/2}L_{k,f} \tag{1}$$

where x_i and x_f are the vectors of the equilibrium Cartesian coordinates in i and f, respectively, M is the diagonal matrix of the atomic masses, and $L_{k,f}$ is the vector of the normal coordinates of the vibrational mode k in terms of mass-weighted Cartesian coordinates. $L_{k,f}$ vectors were obtained from frequency calculations, whereas x vectors are taken from ground-state and excited-state structures. Huang−Rhys (HR) factors, S_k, are then given by

(14) Frisch, M. J.; et al. *Gaussian03*, revision C.02 ed.; Gaussian, Inc.: Wallingford, CT, 2004.
(15) Becke, A. D. *Phys. Rev. A* **1988**, *38*, 3098−3100.
(16) Lee, C. T.; Yang, W. T.; Parr, R. G. *Phys. Rev. B* **1988**, *37*, 785−789.
(17) Becke, A. D. *J. Chem. Phys.* **1993**, *98*, 5648−5652.

(18) *Ampac 8.16*; Semichem Inc.: 2004, Shawnee Mission, KS.
(19) Yet, such scaling of vibrational frequencies for semiempirical techniques may not be valid for all vibrational modes.
(20) Gierschner, J.; Mack, H. G.; Luer, L.; Oelkrug, D. *J. Chem. Phys.* **2002**, *116*, 8596−8609.
(21) Siebrand, W. *J. Chem. Phys.* **1967**, 2571.

$$S_k = \frac{2\pi^2 c}{h} \nu_k (\Delta Q_k)^2 \quad (2)$$

Here, h is Planck's constant, c is the velocity of light, ν_k is the kth frequency of the final state, and ΔQ_k is the projection of geometry change between two states calculated with eq 1. The Franck−Condon (FC) factors are then estimated by the expression[21]

$$F^2_{n0}(k) = \frac{(S_k)^{n_k} e^{-S_k}}{n_k!} \quad (3)$$

F^2_{n0} is the FC factor and n_k is the nth progression of considered mode k in the final state. The vibrational intensity distribution in the absorption and fluorescence spectra was calculated for T → 0 K according to the formula below

$$I(\nu) = f \frac{2}{\gamma} \sqrt{\frac{\ln 2}{\pi}} \sum_{n_1=0}^{\infty} \cdots \sum_{n_p=0}^{\infty} \prod_{k=1}^{p} F^2_{n0}(k) \times$$
$$\exp\left[\frac{-4\ln 2}{\gamma^2}(\nu - \nu_{00} + g\sum_{k=1}^{p} n_k \nu_k)^2\right] \quad (4)$$

where f is the oscillator strength, ν_{00} is the electronic origin, $g = 1$ for emission, $g = -1$ for simulation of absorption spectra, and γ is the line of broadened bandwidth at half-height.

In vibronic spectra simulations, the ground-state structures were obtained by partial optimization of excited-state structures with frozen dihedral angles. The optimized structure of G1-2S with frozen dihedral angles (taken from excited-state geometry parameters) is only 2.4 kcal mol^{-1} higher in energy than the totally relaxed ground-state structure calculated using the same theory and basis set. Furthermore, the absolute average bond length difference between two structures is only 0.002 Å, which means that the ground-state structure with frozen excited-state structure dihedral angles is a good approximation for ground-state geometry in the calculation of ΔQ_k. This approach was utilized to eliminate the effect of torsional movement of thiophene rings in the ground state; otherwise, unrealistically high HR factors could be obtained from eq 2. Nonetheless, such an approximation should cancel out HR factors for low-frequency torsional modes (less than 100 cm^{-1}), though not detrimental in predicting the vibrational progression in these systems. All S_k values corresponding to C−H bending or stretching modes were discarded in estimation of the FC factors.

The effect of temperature on vibronic bands of emission and absorption spectra was approximated by a convolution of low-temperature spectra with a combination of a Gaussian and exponential distribution functions as explained in ref 20. To compare the results of different theoretical approaches, the same functions were used for each molecule in the room-temperature simulation of spectra.

3D Transition Density Plots and CEHPDs. The molecular orbitals generated from the ZINDO method on DFT-optimized geometries were used to construct 3D transition density (TD) plots according to the equation below[22]

$$\rho_{\mu 0}(r) = \sum_{o,u} C_{\mu o u} \varphi_o \varphi_u \quad (5)$$

$C_{\mu o u}$ represents the CI expansion coefficients in the basis of occupied (φ_o) and unoccupied (φ_u) orbitals in the electronic transition. The transition density plots indicate the spatial location of electronic transitions and also provide information about the direction of the transition dipole moment. They are particularly useful to visualize electronic transitions for multiple configurations with CI coefficients of similar magnitude. Nevertheless, TDs only describe the location of

(22) Persson, N. K.; Sun, M.; Kjellberg, P.; Pullerits, T.; Inganas, O. *J. Chem. Phys.* **2005**, *123*.

a transition; they do not provide information about the location of the hole and the excited electron in electronic transitions. To reveal the nature of excited states, we calculated two-dimensional correlated electron−hole probability diagrams (CEHPD) by using eq 6.[23] Each point (x,y) on CEHPDs represents the joint probability of finding the excited electron in the atomic orbitals of the atom x with the corresponding hole in the atomic orbitals of the atom y. Consequently, TDs and CEHPDs show complementary information regarding the changes in the electronic density during an optical transition.

$$\psi(q,r) = \frac{1}{\sqrt{2}} \sum_j C_j^{CI}(c_{uq}^{LCAO} c_{or}^{LCAO} + c_{oq}^{LCAO} c_{ur}^{LCAO})$$
$$|\psi(x,y)|^2 = \sum_{\substack{q \in x \\ r \in y}} |\psi(q,r)|^2 = 1 \quad (6)$$

Vibronic spectra and CEHPDs were generated with in-house programs written in Matlab (version 7.2). All molecular orbital contours were plotted using the ChemCraft (version 1.5) visualization program.

4. Results and Discussion

Ground-State Geometric Properties. The B3LYP hybrid functional along with the 6-31G(d) basis set is known to yield geometries close to experimental observations.[24] Therefore, we will focus on geometries obtained from the B3LYP/6-31G(d) method. DFT-optimized geometries of 3G1-1S, 4G1-1S, and 3G1-2S-CN are illustrated in Figure 3. The optimized 3G1-1S geometry has a bowl-shape structure as it is seen from the side view, and the arms are not coplanar with the phenyl core. The optimized 4G1-1S geometry is quite different than that of 3G1-1S. Due to steric hindrance between the arms at the ortho positions, the dihedral angles between the plane of the core and the adjacent units are quite large (40, 56, 40, and 56° on a clockwise turn). The arms with 40° dihedral angles (para to each other) are expected to have better conjugation with the core compared to those with 56° dihedral angles. Indeed, this is shown to be the case for both absorption and emission profiles of the 4G1-nS series, as will be discussed later.

In contrast to the optimized geometries of 3G1-1S and 4G1-1S, the optimized geometry of 3G1-2S-CN is totally planar. Note that there is no symmetry restriction imposed in our calculations to force planarity in any of the dendrimers studied in this work. The electron-withdrawing nature of the cyanobenzene core is believed to be responsible for such a flat structure, since a test calculation without −CN groups again yielded a bowl-shape structure similar to the optimized geometry of 3G1-1S, though with slightly improved planarity. Interestingly, films prepared from the 4G1-1S dendrimer are amorphous, whereas 3G1-1S-[25] and 3G1-2S-CN-based films show some ordering in the bulk.[26] Geometry optimizations with semiempirical methods showed similar bond lengths and angles to those calculated with DFT-optimized geometries. Nevertheless, PM3-optimized structures showed best agreement with DFT-optimized ones (see Supporting Information for more discussion).

(23) Zojer, E.; Buchacher, P.; Wudl, F.; Cornil, J.; Calbert, J. P.; Bredas, J. L.; Leising, G. *J. Chem. Phys.* **2000**, *113*, 10002−10012.
(24) Tretiak, S.; Mukamel, S. *Chem. Rev.* **2002**, *102*, 3171−3212.
(25) 3G1−1S is amorphous when deposited, but over time it forms highly ordered domains that are visible to the eye and confirmed by the XRD patterns.
(26) Rance, W. L.; Kopidakis, N.; Mitchell, W. J.; Rupert, B. L.; Rumbles, G.; Shaheen, S. E. In preparation.
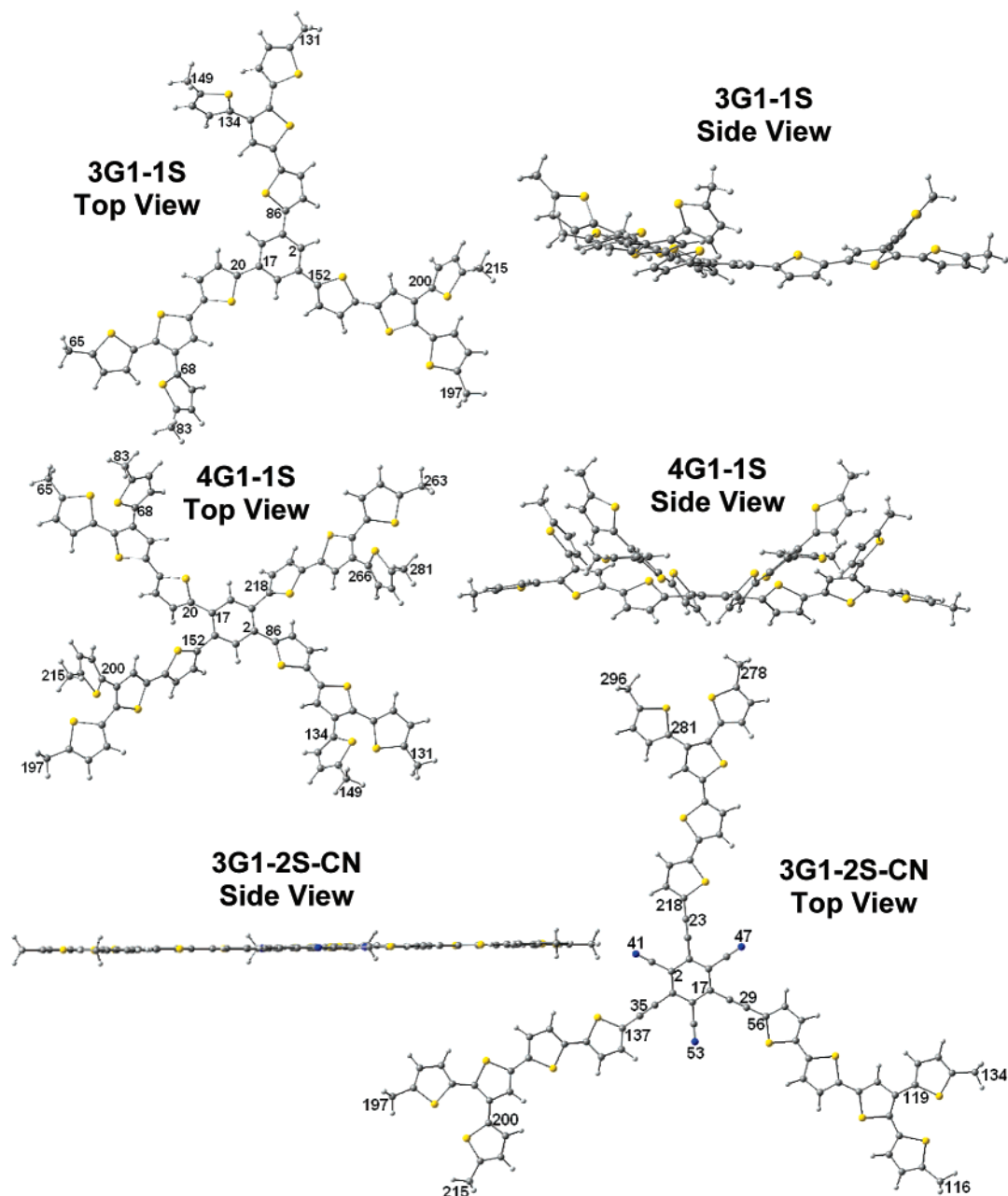
Figure 3. DFT-optimized structures of dendrimers. The numbering is that used in CEHPD diagrams.

Excited-State Geometric Properties. The geometry modifications in the excited state are strongly coupled to vibronic modes in organic molecules. The structural differences between the ground-state and the excited-state geometries indicate the regions where the electronic density is most distorted upon excitation followed by vibrational relaxation. Therefore, a comparison of the ground-state geometry with excited-state geometry would show the parts of the molecule involved in light emission as well as the location of the emitting exciton. The term "cold exciton" will be used for such an exciton mentioned throughout the text, as it is formed after vibrational relaxation to the lowest vibronic mode in the lowest-lying excited state.[27] Similarly, "hot exciton" is generated upon light absorption before any energy relaxation processes occur in higher excited states.

Here RCIS/3-21G, AM1-CI, and PM3-CI were utilized to calculate the excited-state geometries of the 3G1-*n*S series, 4G1-1S, and 3G1-2S-CN. RCIS/3-21G predicted that the lowest-lying singlet-state geometry of 3G1-1S shows significant structural changes in one of the arms, compared to others (see Figure S1, Supporting Information). The backbone of that arm adopts a quinoidal structure with increased planarity between thiophene units connected through the α−α linkage. The increased double-bond character between adjacent thiophene rings hinders the torsional degree of freedom for those bonds.[28] The β-connected, terminal thiophenes do not undergo any structural changes in the excited state, except possessing an increased twist angle of ∼90° with the adjacent thiophene ring. The bond length differences between the excited-state and the

(27) Franco, I.; Tretiak, S. *J. Am. Chem. Soc.* **2004**, *126*, 12130−12140.

(28) The average inter-ring C−C single bond distance between α-linked thiophene units is 1.386 Å, whereas the same distance is 1.440 Å for the other two identical arms.
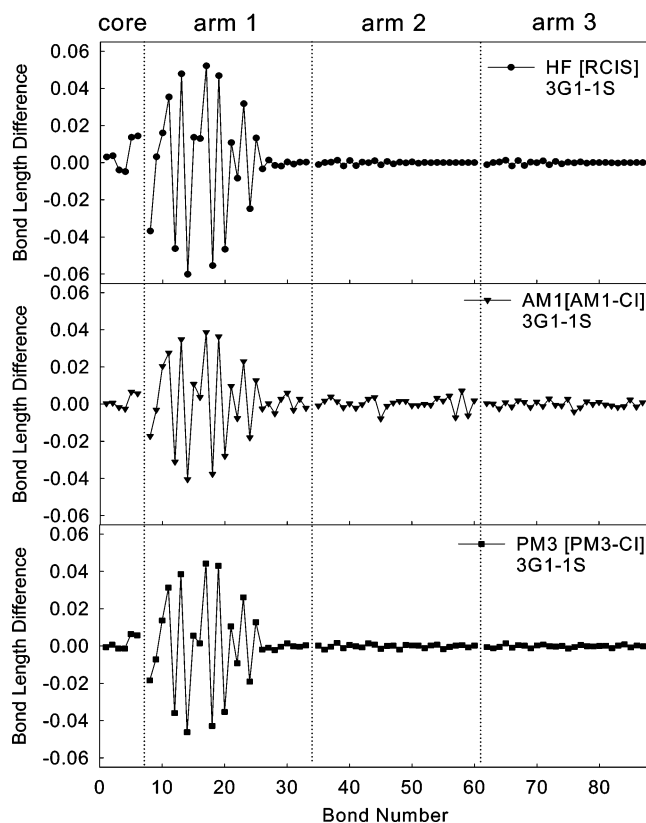
Figure 4. Bond length differences between excited-state and ground-state structures of 3G1-1S calculated with the HF[RCIS], AM1[AM1-CI], and PM3[PM3-CI] methods. Bond numbers follow the same trend as the numbers shown in the optimized structure of 3G1-1S in Figure 3.

ground-state structures of 3G1-1S calculated with HF[RCIS], AM1[AM1-CI], and PM3[PM3-CI] are shown in Figure 4. Note that the RCIS/3-21G optimized geometry is compared to the HF/3-21G optimized ground-state geometry. All methods predict the localization of structural changes on one of the arms. These results suggest the localization of the cold exciton on one of the arms of 3G1-1S delocalized over $\alpha\alpha$- connected thiophenes with some contribution from the phenyl core. The β-connected thiophene is not involved in these processes as also evidenced in thiophene dendrons and dendrimers studied by Xia et al.[9]

A similar analysis for 4G1-1S reveals differences between the HF[RCIS] approach and semiempirical methods (Figure S2, Supporting Information). HF[RCIS] demonstrates the delocalization of a cold exciton over two arms at para positions including the phenyl core, whereas both AM1[AM1-CI] and PM3[PM3-CI] predict the same exciton localization on one of the arms, similar to 3G1-1S. Since a cold exciton is localized on two arms in the HF[RCIS] case, the average C−C single bond length between $\alpha\alpha$- connected thiophene units is now 1.414 Å, larger than the 1.386 Å calculated for 3G1-1S. This finding has important implications in determining which method correctly describes excitonic behavior in 4G1-1S and will be discussed more in the next section.

Absorption and Emission Data. Vertical transition energies were calculated with the TD−DFT and semiempirical methods. The results for absorption transitions are given in Table 1. TD−DFT calculations were carried out on B3LYP/6-31G(d) optimized geometries. Since three-arm dendrimers have C_3 symmetry, the lowest transition energies show 2-fold degeneracy (excited-state symmetry is ^{1}E) along with multiple orbital

transitions for each electronic transition at the same energy. In contrast, four-arm dendrimers and other structures listed in Table 1 exhibit transitions strongly dominated by the HOMO to LUMO levels. Experimental S_0−S_1 transitions were underestimated with the DFT[TD−DFT] approach, whereas semiempirical methods overestimate the same transitions. One remarkable feature is that errors for the DFT[TD−DFT] method increase as the size of the calculated structures gets larger (show some size-consistency), whereas such a trend is absent in semiempirical results. This is a significant drawback for AM1-CI and PM3-CI methods in comparison to TD−DFT despite the fact that they require relatively much less computational resource and time.

Experimental vertical transition energies of G1-2S and 3G1-2S are 3.17 and 2.93 eV, respectively. Thus, going from one arm (without a phenyl core) to a dendrimer results in a red-shift of only 0.24 eV. Now the question remains whether this shift is due to increased π-electron conjugation of thiophenes in the arm with the phenyl core or due to π-system delocalization extended to all arms either partially or as a whole. This question can be answered by comparing the theoretical data obtained for G1-2S and G1-2S (arm w/c), where the latter structure contains the extra phenyl core, which is absent in G1-2S. The calculated red-shift between the two structures is 0.17 eV (close to the shift observed experimentally between G1-2S and 3G1-2S), and this shift can be regarded as a reliable result, since the size of both molecules is very similar. This finding suggests the absence of electronic coupling between the arms and it is consistent with the earlier findings for meta-linked structures where conjugation is disrupted for such molecules.[29−31]

Both experimental and theoretical results identify 3G1-2S-CN as the lowest band gap material among the structures studied in this work. The electron-withdrawing nature of −CN groups is responsible for the decreased transition energy, since removal of these groups (G1-2S-AC (arm w/c): 2.59 eV vs G1-2S-CN (arm w/c): 2.00 eV) drastically increase the vertical absorption energies.

The experimental S_0−S_1 transition energies for 4G1-nS series are almost the same as 3G1-nS series, which is also supported by theoretical results to a great extent.[32] Unlike the 3G1-nS series, the arms in 4G1-nS are in ortho, para, and meta positions, where the ortho and para branching allows electronic coupling between the arms. However, as discussed above, the sterically repulsive forces cause the arms to have large twist angles with the core, which is somewhat detrimental to conjugation over the core. Nonetheless, the onset of absorption in 4G1-nS is red-shifted by ~0.1 eV compared to the onset of absorptions measured for 3G1-nS. This provides, to some extent, an evidence for electronic interactions between the arms, and this issue will be revisited more below in the Spatial Location of Exciton section.

Fluorescence emission values were also calculated with all three methods (Table 2); however, in this instance, the RCIS/3-21G method was used to calculate the excited-state structure

(29) Lupton, J. M.; Samuel, I. D. W.; Burn, P. L.; Mukamel, S. *J. Chem. Phys.* **2002**, *116*, 455−459.
(30) Wu, C.; Malinin, S. V.; Tretiak, S.; Chernyak, V. Y. *Nat. Phys.* **2006**, *2*, 631−635.
(31) Kopelman, R.; Shortreed, M.; Shi, Z. Y.; Tan, W. H.; Xu, Z. F.; Moore, J. S.; BarHaim, A.; Klafter, J. *Phys. Rev. Lett.* **1997**, *78*, 1239−1242.
(32) Mitchell, W. J.; Kopidakis, N.; Ferguson, A. J.; Kose, M. E.; Ginley, D. S.; Rumbles, G.; Shaheen, S. E. In preparation.

Table 1. Experimental and Computed Vertical Absorption Transition Energies Calculated with TD−DFT, AM1-CI, and PM3-CI in Dendrimers and Dendrimer Arms with Core

| structure | exp. abs (eV) S_0–S_1 | DFT[TD–DFT] B3LYP/6-31G(d)// B3LYP/6-31G(d) | | | | AM1[AM1-CI] | | PM3[PM3-CI] | |
		calcd (eV)	ΔE (eV)	major orbital transitions	f^a (a.u.)	calcd (eV)	ΔE (eV)	calcd (eV)	ΔE (eV)
G1-2S	3.17	2.91	−0.16	$H^b \rightarrow L^b$, 100%	0.92	3.50	+0.33	3.65	+0.48
3G1-1S	3.11	2.83	−0.28	H −2 → L, 15% H −1 → L, 38% H → L +1, 38%	1.39^c	3.24	+0.13	3.43	+0.32
				H −2 → L +1, 15% H → L, 38% H → L, 38%	1.39^c				
3G1-2S	2.93	2.52	−0.41	H −2 → L, 12% H −2 → L + 1, 16% H −1 → L, 31% H → L +1, 31%	2.30^c	3.17	+0.24	3.39	+0.46
				H −2 → L +1, 12% H −2 → L, 16% H −1 → L +1, 31% H → L, 31%	2.30^c				
3G1-3S	2.80	2.39	−0.41	H −1 → L +1, 15% H → L, 15% H → L +2, 15% H −2 → L, 31%	2.92^c	3.02	+0.22	3.25	+0.45
				H −1 → L, 15% H −1 → L +2, 15% H → L +1, 15% H −2 → L +1, 31%	2.92^c				
3G1-2S-CN	2.31	1.88	−0.43	H −2 → L, 22% H −1 → L +1, 22% H → L +1, 52%	1.62^c	2.85	+0.54	2.95	+0.64
				H −2 → L +1, 22% H −1 → L, 22% H → L, 52%	1.62^c				
G1-1S (arm w/c)		3.01		H → L, 100%	0.80				
G1-2S (arm w/c)		2.74		H → L, 100%	1.37				
G1-3S (arm w/c)		2.53		H → L, 100%	1.83				
G1-2S-CN (arm w/c)		2.00		H → L, 100%	1.03				
G1-2S-AC (arm w/c)		2.59		H → L, 100%	1.69				
4G1-1S	3.12	2.78	−0.44	H → L, 100%	1.04	3.48	+0.36	3.68	+0.56
4G1-2S	2.94	2.49	−0.45	H → L, 100%	1.51	3.36	+0.42	3.68	+0.74
4G1-3S	2.81	2.32	−0.49	H → L, 97%	2.08	2.99	+0.18	3.51	+0.70
avg. error			−0.38				+0.30		+0.54

^{a} f: computed oscillator strength. ^{b} H: HOMO, L: LUMO. ^{c} There are two degenerate states associated with S_0−S_1 transition.

as an input in TD−DFT calculations. Again, TD−DFT results underestimate the S_1−S_0 transition energies whereas AM1-CI and PM3-CI overestimate the experimental results. Experimental emission energies decrease in both 3G1-*n*S and 4G1-*n*S series as *n* increases.[32] Overall, 4G1-*n*S have lower vertical emission values than 3G1-*n*S, which implies better delocalization of the cold exciton in 4G1-*n*S compared to 3G1-*n*S, a result supported by all of the theoretical methods used in this study. A careful analysis of bond length difference plots of 4G1-1S (Figure S2, Supporting Information) shows more pronounced changes in the bond lengths at the phenyl core and at the other arms as compared to the changes between the excited-state and the

ground-state structures of 3G1-1S (Figure 4). These results imply that cold excitons are more delocalized in the 4G1-*n*S series of dendrimers.

Simulated Excitation and Emission Spectra. To assess the reliability of semiempirical methods in describing the vibronic couplings, we simulated and compared the excitation/emission spectra obtained at different levels of theory. A thorough Franck−Condon treatment of normal modes of electronic states allowed us to estimate Huang−Rhys factors and vibronic progressions as outlined in the Theoretical Approaches section. The simulations include electronic and vibronic states as well as spectral shifts caused by thermally activated torsional motions

Table 2. Experimental and Computed Vertical Fluorescence Transition Energies of Dendrimers and Dendrimers Arms with Core

structure	Exp. em (eV) S_1-S_0	RCIS[TD–DFT] 3-21G//B3LYP/6-31G(d)		AM1-CI		PM3-CI	
		Calcd (eV)	ΔE (eV)	Calcd (eV)	ΔE (eV)	Calcd (eV)	ΔE (eV)
G1-2S	2.61	2.44	−0.17	2.74	+0.13	2.72	+0.11
3G1-1S	2.60	2.45	−0.15	2.82	+0.22	2.71	+0.11
3G1-2S	2.50	2.21	−0.29	2.90	+0.40	2.75	+0.25
3G1-3S	2.38	2.05	−0.33	2.54	+0.16	2.50	+0.12
3G1-2S-CN	1.84	1.87	+0.03	2.46	+0.54	2.38	+0.46
G1-1S (arm w/c)		2.51					
G1-2S (arm w/c)		2.27					
G1-3S (arm w/c)		2.12					
G1-2S-CN (arm w/c)		1.92					
G1-2S-AC (arm w/c)		2.21					
4G1-1S	2.36	2.09	−0.27	2.66	+0.30	2.63	+0.27
4G1-2S	2.32			2.67	+0.35	2.52	+0.20
4G1-3S	2.28			2.59	+0.31	2.47	+0.19
Avg. Error			−0.20		+0.30		+0.21

of the thiophene rings. We neglected any solvent-induced shifts in our simulations as the photoinduced electronic transitions for the calculated structures have little or no charge-transfer character (except for 3G1-2S-CN). A TD−DFT calculation with polarizable continuum model on G1-2S in the presence of dichloromethane predicted a red-shift of only 0.09 eV in the absorption spectrum from the gas-phase calculation, close to the values predicted for solvent dependence of oligothiophene transition energies in solvents with different polarities.[33] We measured both room temperature (RT) and 80 K excitation and emission spectra of G1-2S, 3G1-1S, and 4G1-1S. Low-temperature measurements aimed to resolve vibronic subbands better, which in turn enabled healthier comparison of the simulated vibronic structure. They were also exploited to analyze any possible shift in the spectra due to a change in temperature since thiophenes have low torsional potential for ring rotation.[34,35] The experimental spectra for the G1-2S molecule are shown in the top panel of Figure 5. There are several remarkable features in the spectra: First, the vibronic subbands in emission and excitation spectra are, as expected, better resolved at 80 K compared to the RT spectra. Second, the vibronic subbands in excitation and emission are not mirror-symmetrical, which indicates there are significant differences in the nuclear displacement of the vibronic modes in the electronic S_0 and S_1 states. Third, the intensity of vibronic subbands changes with temperature, implying some structural changes with the temperature that can be attributed to the frozen environment of the stationary solvent molecules at 80 K that restricts the movement of molecules in the glassy matrix environment. Fourth, the excitation spectra significantly blue shift at higher temperature, although such a shift is less evident in the emission spectra. The temperature evolution of excitation spectra is commonly seen in oligothiophenes[36] and some other conjugated molecules.[20] This is due to low torsional potential of attached thiophene rings,[35,37] which has a disruptive impact on the π-electron delocalization along the conjugated backbone as the temperature increases.
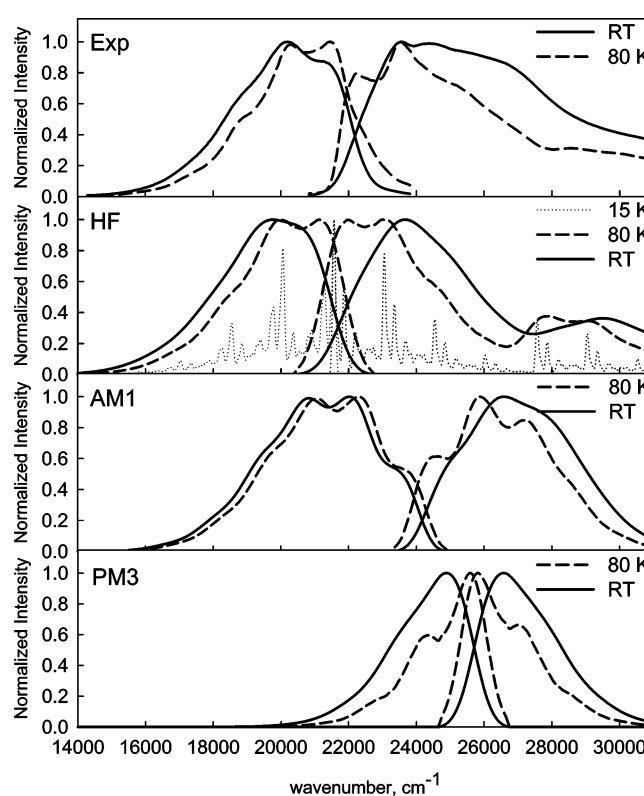
Figure 5. Experimental (in 2-methyl THF) and simulated (HF, AM1, PM3) emission/excitation spectra of G1-2S determined at room temperature (RT) and at 80 K.

The simulated spectra of G1-2S with HF[RCIS], AM1[AM1-CI], and PM3[PM3-CI] are illustrated in the lower panels of Figure 5. The electronic origin is estimated from the vertical transition energies listed in Table 1 and 2 by assuming the same equilibration energies present at both the excited and ground states. The line bandwidths were around ~0.1 eV and slightly varied from technique to technique to get similar vibronic bandwidths to the experiment. Overall, the HF[RCIS] method gives the best results when compared to experiment, both in terms of band positions and vibronic structure.[38] To get a better

(33) Meng, S.; Ma, J.; Jiang, Y. S. *J. Phys. Chem. B* **2007**.
(34) Breza, M.; Lukes, V.; Vrabel, I. *J. Mol. Struct.: THEOCHEM* **2001**, *572*, 151−160.
(35) Zade, S. S.; Bendikov, M. *Chem.−Eur. J.* **2007**, *13*, 3688−3700.
(36) Gierschner, J.; Mack, H. G.; Egelhaaf, H. J.; Schweizer, S.; Doser, B.; Oelkrug, D. *Synth. Met.* **2003**, *138*, 311−315.
(37) Diaz-Quijada, G. A.; Weinberg, N.; Holdcroft, S.; Pinto, B. M. *J. Phys. Chem. A* **2002**, *106*, 1266−1276.

(38) Sancho-Garcia, J. C.; Bredas, J. L.; Beljonne, D.; Cornil, J.; Martinez-Alvarez, R.; Hanack, M.; Poulsen, L.; Gierschner, J.; Mack, H. G.; Egelhaaf, H. J.; Oelkrug, D. *J. Phys. Chem. B* **2005**, *109*, 4872−4880.
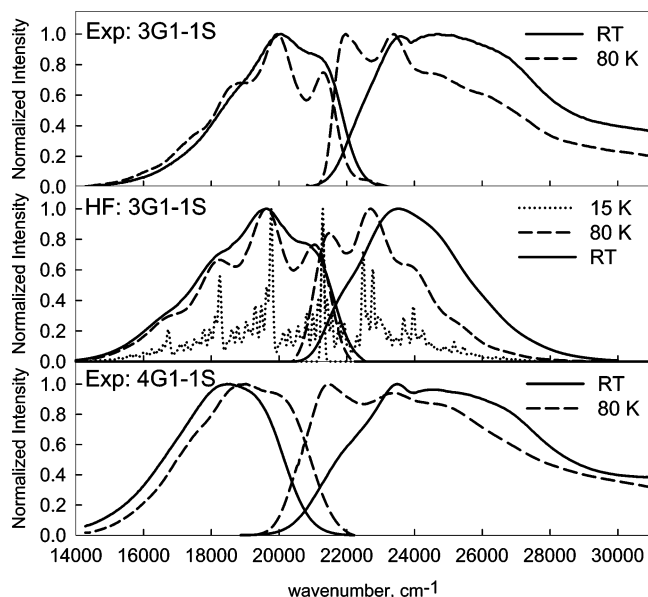
Figure 6. Experimental (in 2-methyl THF) and simulated (HF, 3G1-1S only) emission/excitation spectra of 3G1-1S and 4G1-1S determined at room temperature (RT) and at 80 K. See Figures S3 and S4 in Supporting Information for simulations performed with AM1 and PM3 results.

Table 3. Experimental and Computed Lifetimes of Dendrimers

structure	fluorescence lifetime, τ_F/ps	natural lifetime, τ_R/ns	DFT, calcd τ_R/ns	AM1, calcd τ_R/ns	PM3, calcd τ_R/ns
3G1-1S	250 ± 10	2.9 ± 0.2	1.28	0.96	1.23
3G1-2S	585 ± 20	2.4 ± 0.2	1.11	0.77	0.97
3G1-3S	800 ± 10	2.3 ± 0.3	1.11	0.90	1.05
4G1-1S	560 ± 10	3.4 ± 0.4	1.35	1.30	1.46
4G1-2S	645 ± 15	3.1 ± 0.4		1.00	1.30
4G1-3S	675 ± 75	4.5 ± 1.3		0.92	1.27

temperature change causes only line broadening in the fluorescence vibronic subbands of 3G1-1S. Likewise, one can conclude a comparatively larger cold exciton size in 4G1-1S than in 3G1-1S. All these experimental findings imply that the excited-state structure of 4G1-1S would be correctly described with RCIS rather than AM-CI and PM3-CI methods, where semiempirical methods predict the cold exciton to be confined to only one arm for both 4G1-1S and 3G1-1S (see Figure 4 and Figure S2, Supporting Information).

Theoretical Lifetimes. To calculate the theoretical natural radiative lifetimes, we used eq 7 to estimate the radiative rate constant, which is described in ref 38 after manipulation of the Strickler and Berg expression.[41]

$$k_r = 0.667 n^2 f \frac{E_{S_1-S_0}^3}{E_{S_0-S_1}} \qquad (7)$$

Here, n is the refractive index of the solvent used in the experiments, f is the oscillator strength, $E_{S_1-S_0}$ and $E_{S_0-S_1}$ are the vertical fluorescence and absorption transition energies, respectively, in cm^{-1} units. The inverse of k_r yields the natural radiative lifetime and can be readily compared to experimental data if both the fluorescence quantum yield and fluorescence lifetime are known for the molecule in question. Table 3 lists both experimental and calculated natural lifetimes from the transition energies obtained from the DFT and semiempirical methods. The calculated lifetimes underestimate the experimental ones by a few nanoseconds; however, there is a reasonably good agreement between experimental data and theoretical results and all are consistent with a fully allowed radiative transition. The variation of DFT-calculated lifetimes specifically parallel experimental lifetimes (Figure S5, Supporting Information), though such correlation is less pronounced for the calculated semiempirical lifetimes when compared to experimental ones.

Charge Distribution in Charged Dendrimers and Reorganization Energies. Both the location and extension of polarons (radical ion structures in conjugated chains) are important to reveal the nature of the charge carriers in electrically conducting polymers and oligomers. Considering that vibronic modes strongly couple with the charged state to lead to charge localization, accompanied by a structural distortion over the conjugated chain, it is then possible to estimate the size and location of polaronic states.[42] Delocalized polarons are vital to maximize the electronic interaction between the ions and the neutral molecules to facilitate efficient charge transport in photovoltaic devices.

prediction for the high-energy component of the experimental excitation spectra, we included Franck−Condon factors for the excited-state with the next-largest oscillator strength. The fine vibronic spectrum is also given for the HF[RCIS] case with ~0.01 eV line broadening that would presumably be obtained at around 15 K.[36] The computed spectra in all three methods show almost mirror symmetry between excitation and emission profiles.[39] AM1[AM1-CI] estimates large equilibration energies with relatively incorrect vibronic subband intensities. In contrast, the magnitudes of the HR factors obtained from the PM3[PM3-CI] approach are much less than the experimental ones, and hence, equilibration energies for this approach are much smaller than the ones estimated by the other theoretical methods.

Figure 6 shows the simulated excitation and emission spectra of 3G1-1S with the HF[RCIS] approach, which does a much better job in evaluation of both vibronic subbands and their relative intensities compared to semiempirical ones (see Figure S3, Supporting Information). The higher energy portion of excitation spectra contains transitions to higher lying excited states and these were not simulated. We performed the same simulations for the 4G1-1S dendrimer (Figure S4, Supporting Information) with AM1[AM1-CI] and PM3[PM3-CI] methods; however, their predictions are not as good.[40] One of the distinct features in Figure 6 is the strong experimental spectral shift in 4G1-1S spectra, upon temperature change from 80 K to RT. The shift in the excitation spectrum of 4G1-1S is larger than that observed for 3G1-1S, suggesting the existence of relatively extended delocalization of the hot exciton in 4G1-1S which, in turn, is strongly affected by torsional motion of the thiophene rings with temperature change. Another important feature is that the emission bands shifted as a whole in 4G1-1S, whereas the same

(39) This is probably an artifact of simulations that employ optimized ground-state structures with frozen dihedral angles taken from excited-state structures. Nevertheless, such an approximation does give a very good result for the emission spectrum using the HF[RCIS] method.

(40) The HF[RCIS] method was not carried out in this case due to limitations in our computational resources. Yet, AM1[AM1-CI] and PM3[PM3-CI] methods can be readily applied for 4G1−1S and even much larger structures.

(41) Strickler, S. J.; Berg, R. A. *J. Chem. Phys.* **1962**, 814.

(42) Moro, G.; Scalmani, G.; Cosentino, U.; Pitea, D. *Synth. Met.* **2000**, *108*, 165−172.

We investigated the delocalization of positive and negative charges in radical cations and anions of dendrimers with the data acquired from Mulliken population analysis in the DFT calculations. The results indicate extensive delocalization of positive and negative charges over the dendrimers, except for 3G1-2S-CN, where negative charge is mostly localized on the cyanobenzene core (see Figure S6 in Supporting Information along with more discussion). In accordance with charge distribution, the radical ion geometries of dendrimers are slightly different than those of neutral ones. The changes in the bond lengths show a trend for a quinoidal structure. However, due to extensive delocalization of charges over the molecules, the bond length changes are small, retaining aromaticity in the rings. G1-2S, on the other hand, adopts a quinoidal structure along α-linked thiophenes in both radical cation and anion geometries.

The motion of the carriers in an amorphous organic film can be modeled as a sequence of uncorrelated hops. The self-exchange electron-transfer reaction from a charged species to an adjacent neutral unit is controlled by self-exchange electron-transfer hopping rate, which is given by[43,44]

$$k_{ET} = A \exp[-\lambda/4k_bT] \qquad (8)$$

The factor A depends on the strength of electronic coupling between adjacent units, and in our case, we assume that the coupling is weak due to little or absence of ordering in the dendrimer/PCBM blends. On the other hand, even in an amorphous dendrimer/PCBM blend the factor A might play a significant role in the determination of the electron-transfer rate, given that polarons are very well delocalized over the arms and the core. The reorganization energy, λ, is another key parameter that controls the rate constant for electron-transfer reactions and can be divided into two terms, λ_{med} and λ_{int}. λ_{med} accounts for the effect of the polarized medium on charge transfer whereas λ_{int} (internal reorganization energy) is a measure of structural changes between ionic and neutral states.[45] In the solid-state films of the dendrimer/PCBM blends, we do not expect λ_{med} to be the dominant contributor to λ, due to the low dielectric constant of medium. Therefore, we will focus our discussion around λ_{int}, which has been calculated according to the following formula[46]

$$\lambda_{int} = [E^{\pm}{}_{g(0)} - E^{\pm}{}_{g(\pm)}] + [E^{0}{}_{g(\pm)} - E^{0}{}_{g(0)}] \qquad (9)$$

$E^{\pm}{}_{g(0)}$ is the energy of the cation (anion) calculated with the optimized structure of the neutral molecule. Similarly, $E^{\pm}{}_{g(\pm)}$ is the energy of the cation (anion) calculated with the optimized cation (anion) structure, $E^{0}{}_{g(\pm)}$ is the energy of the neutral molecule calculated at the cationic (anionic) state, and finally $E^{0}{}_{g(0)}$ is the energy of the neutral molecule at ground state. To achieve a high electron-transfer rate, one should maximize factor A and minimize λ (eq 8). As indicated above, the electronic coupling is probably weak in dendrimer/PCBM blends; therefore, the carrier mobility in these films is possibly governed by the magnitude of the reorganization energy. Table 4 lists the

(43) Barbara, P. F.; Meyer, T. J.; Ratner, M. A. *J. Phys. Chem.* **1996**, *100*, 13148−13168.
(44) Demadis, K. D.; Hartshorn, C. M.; Meyer, T. J. *Chem. Rev.* **2001**, *101*, 2655−2685.
(45) Hutchison, G. R.; Ratner, M. A.; Marks, T. J. *J. Am. Chem. Soc.* **2005**, *127*, 2339−2350.
(46) Fratiloiu, S.; Senthilkumar, K.; Grozema, F. C.; Christian-Pandya, H.; Niazimbetova, Z. I.; Bhandari, Y. J.; Galvin, M. E.; Siebbeles, L. D. A. *Chem. Mater.* **2006**, *18*, 2118−2129.
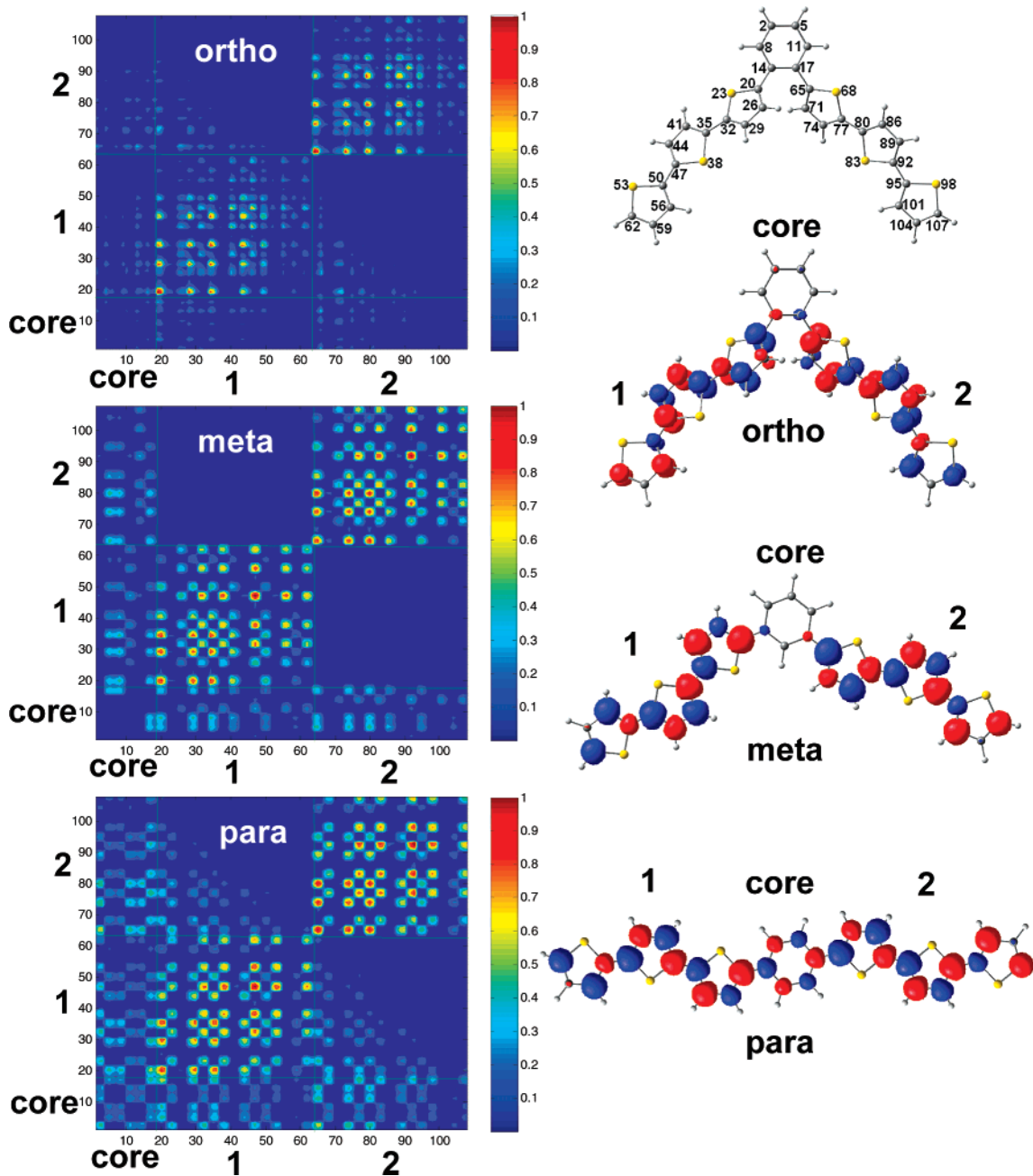
Table 4. Calculated Intramolecular Reorganization Energies for Hole and Electron Transport along with Experimental Short-Circuit Current Values for PV Devices

structure	λ_{hole} (eV)	$\lambda_{electron}$ (eV)	λ_{total} (eV)	$J_{SC}{}^{a}$ (mA/cm²)
G1-2S	0.368	0.355	0.723	
3G1-1S	0.149	0.151	0.300	0.64
3G1-2S	0.060	0.116	0.176	*b*
3G1-3S	0.182	0.105	0.287	*b*
4G1-1S	0.215	0.242	0.457	0.21
4G1-2S	0.073	0.187	0.261	0.68
4G1-3S	0.108	0.135	0.243	1.65
3G1-2S-CN	0.015	0.104	0.119	2.54

a Measured for devices prepared under identical conditions with the same PCBM loading. *b* Dendrimers 3G1-2S and 3G1-3S were too insoluble for device studies.

calculated internal reorganization energies for both electrons and holes, and their sum is given as well to make a comparison from a standpoint of total charge carrier mobility.

The short-circuit current density, J_{SC}, (for the same loading of PCBM in the device) from device characterization[6] is given to compare the reorganization energies with the conductivity measurements. Three features are striking in Table 4. First, the smaller values of the reorganization energies of dendrimers compared to G1-2S are consistent with a higher degree of delocalization of the charges over the dendrimers. Second, as λ_{total} increases, J_{SC} decreases, i.e., the electron-transfer rate picture depicted by eq 8 is consistent with the experimental data. Third, λ_{hole} and $\lambda_{electron}$ are not always of the same magnitude, indicating different carrier mobilities for holes and electrons with varying size of dendrimer. Specifically, high charge carrier mobility of holes for 3G1-2S-CN is more marked than its electron mobility. This is not unexpected, as excess negative charge is mostly localized over the cyanobenzene core (Figure S6, Supporting Information) for this dendrimer. Further experimental investigations of the electron and hole mobility in thin films of the dendrimers are underway to assess the relative contributions of reorganization energy and energetic and spatial disorder to the mobility of photogenerated carriers.

Spatial Location of Excitons. Geometrical changes in the excited state associated with careful analyses of absorption and emission data have provided some insight to the size and the location of excitons in these dendrimers. Yet, a more complete picture can be obtained through 3D transition density plots (TDs) combined with correlated electron−hole pair diagrams (CEHPDs). TDs for three-arm dendrimers revealed that arms are predominantly involved in absorption whereas there is almost no transition density over the core (Figure S7, Supporting Information). The transition densities for emission, however, are localized over one arm including the core, in agreement with the geometrical changes shown in Figure 4 for 3G1-1S (see Supporting Information for more discussion on TDs).

Before analyzing the excitonic behavior in dendrimers, we analyze the effect of ortho, meta, and para substitution in two-arm phenyl-cored structures as shown by the CEHPDs in Figure 7. Ortho substitution mostly favors the localization of a hot exciton over the arm. There is, however, still some correlation seen in box (1−2) (or (2−1)) that points to a small probability of electron−hole coherence over two arms. Few coefficients are seen for core−core, core−1, and core−2 correlations. Therefore, the core is very weakly coupled to exciton diffusion, most probably due to twisting of adjacent

Figure 7. Correlated electron−hole pair diagrams (CEHPDs) of hot exciton (left) with 3D transition density plots of the corresponding two-arm structure (right). Top right structure shows the numbering used for the axes in all diagrams.

thiophene units with the phenyl core because of steric hindrance which diminishes effective electronic coupling. Meta substitution causes localization of an exciton over the arm and to some extent over the core.[47] The absence of most of the coefficients in the core−core box, and conversely, the existence of them in the core−1 and core−2 boxes suggests a charge-transfer type photoexcitation from the arm to the core. Since there are no correlation coefficients in box (1−2) (or box (2−1)), the exciton is strictly limited to the arms and the core. Therefore, the electron (or hole) is not carried beyond one arm as compared to ortho substitution. Para substitution allows the exciton to delocalize over both arms and through the phenyl core, which

mediates such delocalization. In all three cases, para and ortho substitution enables excitonic delocalization over the whole structure whereas meta substitution localizes excitations to arms without any electronic coupling between them. These findings have important implications to explain the exciton localization/delocalization behavior seen in 3G1-*n*S and 4G1-*n*S where all types of substitutions exist between the arms.

Figure 8 illustrates the CEHPDs for both the hot exciton and cold exciton in three-arm dendrimers. These dendrimers have only meta-substituted arms, and calculations on spatial location of hot excitons show a complicated and different behavior for each dendrimer in question. CEHPD for 3G1-1S shows that hot exciton is localized on two arms and the core with coefficients on the second arm being larger than the first. Arms also interact

(47) Pogantsch, A.; Mahler, A. K.; Hayn, G.; Saf, R.; Stelzer, F.; List, E. J. W.; Bredas, J. L.; Zojer, E. *Chem. Phys.* **2004**, *297*, 143−151.
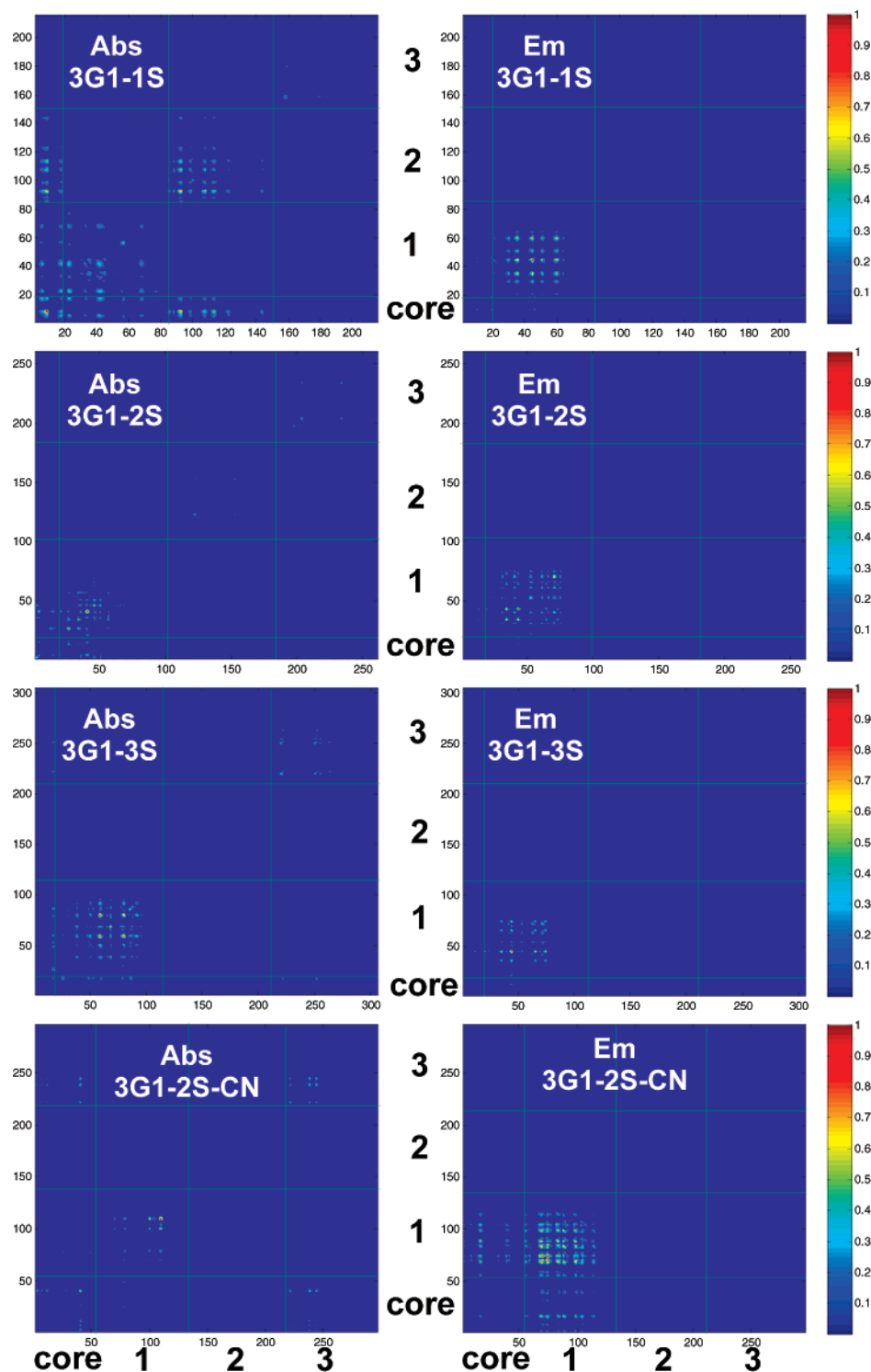
Figure 8. Correlated electron−hole pair diagrams of hot exciton (left) and cold exciton (right) for dendrimers 3G1-*n*S and 3G1-2S-CN. See Figure 3 for numbering.

with the core but not with each other as expected in meta-substituted conjugated segments.[47] 3G1-2S, however, exhibits localization of the hot exciton over only one arm with some contribution from the core. 3G1-3S is similar to 3G1-2S, as the exciton is completely localized on one arm but in this case the phenyl core is not involved in the photoexcited state. The interpretation of these results may not be as complicated as it seems. The hot exciton is spatially delocalized over five α-connected thiophene units in the first arm of 3G1-3S, which

appears to be the size needed for such a photoexcitation. As the size of the dendrimer decreases (going from *n* = 3 to *n* = 1), the exciton uses the core for spatial rearrangement (3G1-2S, four α-connected thiophene units in one arm) or even delocalizes over two arms (3G1-1S, three α-connected thiophene units in one arm) for the same purpose. CEHPD for 3G1-2S-CN shows largest coefficients in arm 1 and some smaller ones on arm 3 and on some portion of the core. The coefficients on arm 1 and arm 3−core are typical π−π* type
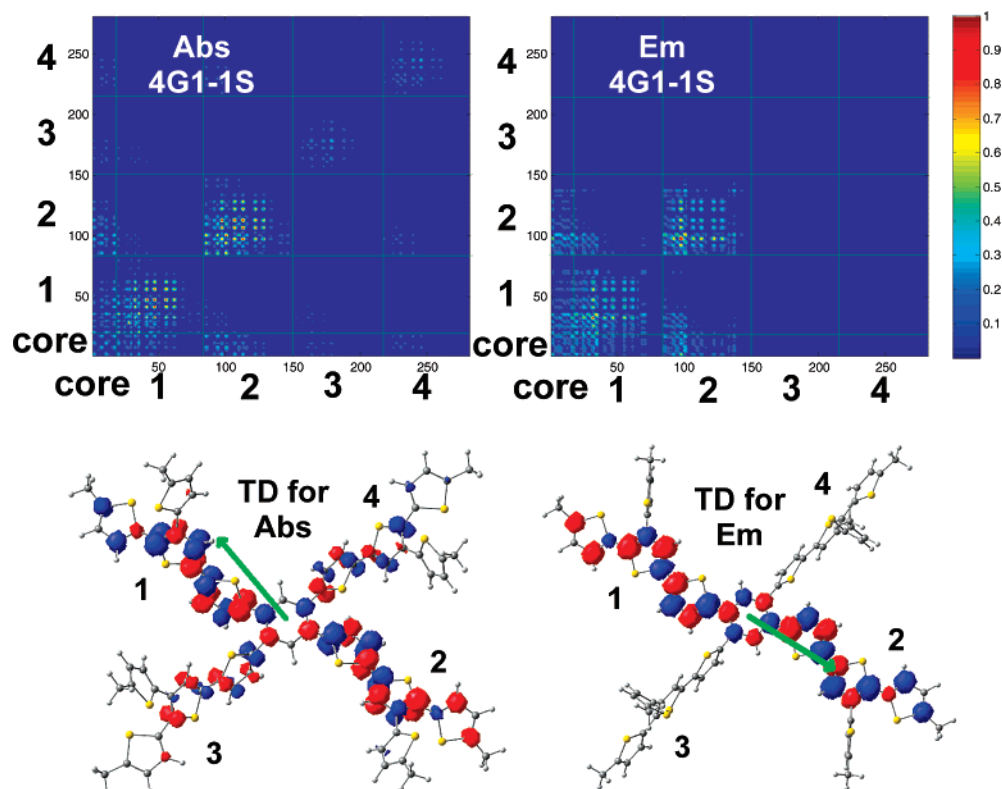
Figure 9. (Top) Correlated electron−hole pair diagrams of hot exciton (left) and of cold exciton (right) for 4G1-1S. (Bottom) 3D transition density plots of hot exciton (left) and of cold exciton (right) for 4G1-1S. See Figure 3 for numbering.

transitions. Yet, there is a charge-transfer type of shift of electronic density within the core in this electronic transition that is also supported by the experiments performed in solvents with different polarities.[48]

Cold excitons (Figure 8, right column) are all localized over three α-connected thiophene units on one of the arms in 3G1-*n*S series with $\pi-\pi^*$ character. On the other hand, 3G1-2S-CN shows significant charge transfer from arm 1 to the core. The absence of coefficients in the core−core box is an indication of a pure charge-transfer transition. Both absorption and emission data in different polarity solvents support our theoretical findings based on CEHPDs.[49] Furthermore, the agreement between the experiment and the theory also suggests the validity of the ZINDO approach used in the calculation of CEHPDs to describe the nature of the photoexcited processes occurring in these macromolecules.

Finally, we discuss CEHPDs for the 4G1-1S dendrimer that has arms situated at ortho, meta, and para positions to each other. CEHPDs for absorption and emission along with the corresponding transition density plots are given in Figure 9. In the case of absorption, the largest coefficients are seen in the diagonal boxes, especially on arm 1 and arm 2. Note that arms

1 and 2, and 3 and 4, are in para positions to each other. The core is also involved in exciton delocalization on arms 1 and 2. There are small coefficients in the (1−2) and (1−3) boxes where these arms are located at para and ortho positions, respectively. However, there are no coefficients in the (1−4) box for the arms at meta positions. The cold exciton is localized over arms 1 and 2, and also the core.

In summary, CEHPDs indicated that hot excitons are more delocalized over the calculated structures compared to cold ones. The relative positions of arms in the dendrimers determine the nature of excitonic behavior; in particular, meta substitutions inhibit interaction of arms between each other. Steric hindrance also causes excitonic localization due to weak electronic coupling between nonplanar units. All these results confirm and support the conclusions drawn in the previous sections.

5. Conclusions

Electronic structure calculations on conjugated polymers and related structures are essential to understand the photophysics of these materials that would lead to the synthesis of novel materials to be used in many different areas. *Ab initio* and semiempirical theoretical methods are important tools in this regard. This work was aimed at elucidating the photophysical properties of first generation three-arm and four-arm dendrimers and also to evaluate the predictive power of different theoretical approaches. Although semiempirical methods are attractive and much faster than *ab initio* methods, the results obtained did not agree as well with the ones obtained from DFT and HF methods. Vertical transition energies, excited-state geometries, and vibronic spectra are better predicted with *ab initio* methods. Reorganization energies were found to correlate well with the experimental short-circuit data of devices, and they most likely

(48) We measured the absorption spectra of 3G1-2S-CN in THF and DCM (slightly more polar than THF) to test this theoretical finding. Absorption maximum of 3G1-2S-CN in DCM is red-shifted by ∼0.05 eV compared to the one collected in THF. The same experiments for 3G1-2S dendrimer resulted in no shift in the absorption spectra, suggesting the absence of any charge transfer type transition in photoexcitation process. Therefore, 3G1-2S-CN shows some charge transfer character in photoexcitation unlike the other dendrimers as verified by both experiment and theory.
(49) To verify this theoretical result, we again compared the emission spectra of 3G1-2S-CN collected in THF and in DCM. The emission maximum of 3G1-2S-CN fluorescence in DCM showed a 0.08 eV red-shift relative to that measured in THF solution. In a control experiment, the emission of 3G1-2S was measured in the same solvents, and the spectra showed a red-shift of only ∼0.01 eV.

play an important role for charge transport in these materials. Hot excitons are more delocalized than cold ones, in agreement with the calculated structural changes in the excited state. The results suggest better delocalization of hot excitons in the 4G1-nS dendrimers as compared to the 3G1-nS dendrimers. Delocalized excitons are needed for efficient electronic coupling between the molecules in charge-transfer reactions. As a result, the charge mobility and device efficiencies can be further improved by a proper choice of substitution scheme and size of the dendrimer as well as the use of groups to decrease the band gap for increased sunlight absorption. In the view of the good agreement between the experiment and the theory, theoretical methods used here provide valuable, cost-effective, and reliable tools to design new materials with optimized properties for OPV applications.

Supporting Information Available: Complete reference 14, more discussions on the sections "Ground-State Geometric Properties", "Charge Distribution in Charged Dendrimers and Reorganization Energies", and "Spatial Location of Excitons", figures include excited-state structures of 3G1-1S, 4G1-1S, and 3G1-2S-CN, bond length difference plots of excited-state and ground-state structures of 4G1-1S, simulated and experimental emission/excitation spectra of 3G1-1S and 4G1-1S, plot of experimental lifetimes vs calculated lifetimes of dendrimers with various methods, excess positive and negative charge distribution in dendrimers and in G1-2S, isodensity transition density plots for both absorption and emission in three-arm dendrimers, Cartesian coordinates, and DFT absolute energies of calculated dendrimers. This material is available free of charge via the Internet at http://pubs.acs.org.

JA073455Y